Appl. Phys. A (2014) 116:555–560
DOI 10.1007/s00339-014-8522-0

Applied Physics A
Materials Science & Processing

RAPID COMMUNICATION

Quantifying the quality of femtosecond laser ablation of graphene

Ramazan Sahin · Selcuk Akturk · Ergun Simsek

Received: 14 February 2014 / Accepted: 15 May 2014 / Published online: 3 June 2014

Abstract The influence of beam intensity on laser ablation quality and ablation size is experimentally studied on graphene-coated silicon/silicon dioxide substrates. With an amplified femtosecond-pulsed laser system, by systematically decreasing the average power, periodic stripes with decreasing widths are ablated. Histogram analyses of the untouched and ablated regions of scanning electron microscope images of the fabricated structures make it possible to quantify the ablation quality. These analyses reveal that submicron ablation can be achieved while maintaining 75 % ablation accuracy by adjusting the beam intensity around the ablation threshold.

1 Introduction

Graphene micro- and nano-structures are considered potential building blocks for future opto-electronic devices [1–5]. The standard lithography assisted cutting approaches offer fabrication scalability and more control on their sizes, shapes and positions [6–8]. However, because of the fabrication complexity of the top-down techniques, the facile production of graphene nano-structures remains challenging. Pulsed laser ablation [9–19] might be a simple yet efficient alternative technique compared to standard lithographic fabrication techniques, which require a photoresist for mask layer generation. In particular, femtosecond (fs) laser ablation provides high quality and repeatable structures due to its non-thermal nature.

In one of the earliest experimental works in this domain, Zhang et al. [10] develop a novel method to fabricate micrometer-sized shapes on graphene oxide films using fs-laser ablation. They also show that the electric resistivity and conductivity of patterned graphene have strong dependences on output power of the fs-laser. In another pioneering work, Kalita et al. [11] use the fs-laser ablation method to produce 5 μm wide graphene stripes on glass substrate. The Raman spectra taken from the ablation region indicate an increase of disorder, yet no formation of amorphous carbon. Dhar et al. [12] study the influence of layer number (for multilayered graphene flakes) on the ablation threshold energy density, and they find that the ablation threshold energy density increases for decreasing layer numbers of graphene originating from the dimensional crossover of the specific heat. Zhang et al. obtain 25 μm wide channels of graphene oxide, separated by <2 μm ablation gaps, on glass substrates using direct fs-laser cutting [13]. A detailed study of graphene ablation mechanisms under single-pulse and multi-pulse irradiation conditions is performed by Roberts et al. [14]. For single-pulse irradiation, a sharp and repeatable ablation threshold and microscopically clean ablation edges are measured. It is also observed that, on multi-shot irradiation, fluences well below the ablation threshold can yield cumulative defect formation and eventual ablation. In the multi-shot irradiation regime, sub-100 nm resolution is demonstrated [15]. In this latter work, the focused laser beam profile is also brought to doughnut shape, thereby yielding sub-diffraction limit nano-ribbons. In an alternative approach, Yoo et al. [16] utilize single-pulse fs-laser ablation for generation of graphene folds on SiO_2/Si substrate. The folds exhibit self-formation of graphene ribbons as small as

R. Sahin · S. Akturk
Department of Physics Engineering, Istanbul Technical University, 34469 Maslak, Istanbul, Turkey

E. Simsek (✉)
Department of Electrical and Computer Engineering, The George Washington University, Washington, DC 20052, USA
e-mail: simsek@gwu.edu

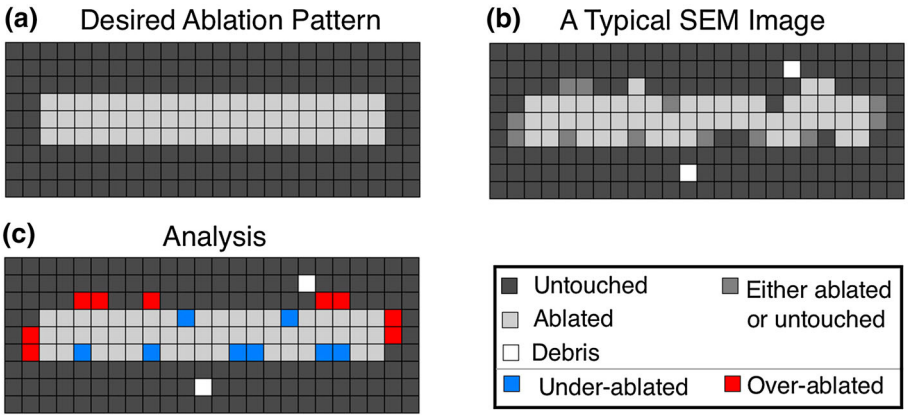

Fig. 1 Sketches of **a** an idealistic and **b** realistic ablated stripe, where *light gray* and *white regions* are the ablated spots and debris, respectively. **c** Under-ablated and over-ablated spots of the realistic case are colored *blue* and *red*, respectively

200 nm around the laser spot. Currie et al. [17] quantify the damage caused by fs-laser pulses in single-layer graphene on sapphire, and they conclude that the size of the damaged area has a linear correlation with the optical fluence.

Although the best fs ablation resolution observed to date is obtained in multi-pulse exposure [15], this regime requires high-numerical aperture focusing (hence very precise sample positioning) and can compromise the purity of the graphene [14]. Our recent studies indicate that fs pulses with Bessel beam profiles provide significant advantages on thin-film type structures [19–21]. Due to their diffraction-free nature, Bessel beams have much longer focal regions (compared to Gaussian beams of same spot size) and the beam size stay unchanged within the focal zone. In [19], we apply the Bessel beam nano-structuring method for patterning of graphene surfaces and show that maskless nanometer size resolution and periodic structures can be produced in a controllable way on single-layer graphene in ambient conditions. Moreover, Raman studies reveal that proper adjustment of sample translation speed allows almost complete removal of graphene, while leaving the substrate totally intact, in the single-pulse-ablation regime. In this work, we examine the quality and completeness of this process as a function of laser average power (hence beam intensity) as follows.

When beam intensity is increased, one would expect an increase in the ablation quality as long as the pulse energy density is between the ablation threshold densities of the graphene and substrate materials, which are Si and SiO_2 in our case. However, it is very well known that the ablation process is imperfect especially near the ablation threshold regime used for nano-machining, because of shot-to-shot variations in pulse energy, overall stability of the setup and uniformity of sample. As depicted in Fig. 1, a scanning electron microscope (SEM) image of an ablated sample shows 3 primary forms of deviation from the intended ablation pattern.

- Under-ablation, mostly due to shot-to-shot instabilities, wherein graphene targeted for ablation is not removed completely,
- Over-ablation, mostly due to unwanted vibrations, wherein unintended regions are ablated, and
- Debris (resulting from partial re-solidification of ablated material).

With these defects in mind, there are two fundamental questions to be addressed: (1) How can we accurately determine which pixels of an SEM image belong to successfully, under, or over-ablated regions, and (2) how can we use that information to quantify the overall ablation quality?

This paper is organized as follows. First, the experimental method to ablate graphene-coated Si-SiO_2 substrates is explained, and an example SEM image of a typical ablated sample is presented. Then, a simple procedure to analyze the SEM images of the ablated samples is described, and a formula to calculate the ablation figure of merit (AFOM) is developed. Finally, we discuss the outcomes of our analyses and conclude.

2 Laser ablation

The commercial single-layer graphene used in the experiments (purchased from Graphene Supermarket) is first grown on copper foils and then transferred to Si/SiO_2 substrate using a polymethyl methacrylate-assisted transfer method. The SiO_2 layer is 285 nm thick, and the surface area of the whole sample is 1 cm^2. Prior to ablation, Raman microscopy measurements are performed with a 532 nm laser source at room temperature, using the method provided in [22] to verify that the samples consist of single-layer graphene. However, pre-ablation SEM images clearly show some cracks and tears, probably created during the transfer process, while some of the post-ablation SEM images depict large areas of over-ablation, probably due to enhanced field by oxidized metal particulates trapped at the graphene/substrate interface. All of the fabricated samples showing these kinds of defects are omitted in our analyses.

The laser source used for ablation is a chirped-pulse amplification system (Amplitude Systemes, s-Pulse),

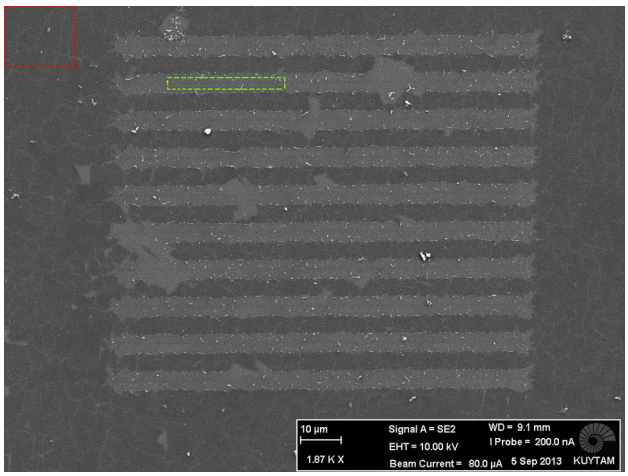

Fig. 2 SEM image of a micro-slit array written by fs-laser Bessel beam ablation. *Lighter* regions are the ablated spots. Regions marked by *red* and *green dashed lines* are used as reference regions for the histogram analysis

producing 550-fs pulses at 1 kHz repetition rate, at a center wavelength of 1030 nm. The spectral bandwidth of the pulses is ~ 2 nm with a very flat spectral phase. The third harmonic of the laser ($\lambda = 343$ nm) is generated through consequent second harmonic and sum-frequency generations. The laser energy is controlled with a waveplate and a polarizer. The Gaussian laser output beam is converted to a Bessel beam with a 40°-base angle axicon. Since the Bessel beam central spot size is proportional to $\lambda/\sin\beta$, (where β is the half cone angle after axicon) using third harmonic wavelength improves ablation resolution significantly. We measure the central spot size (full width at half maximum) as 235 nm, in close match with the calculated value of 230 nm. The longitudinal depth of Bessel zone is 1.5 mm, providing a convenient range for sample positioning.

The sample is scanned under laser illumination by a piezostage (Mad City Labs, Nano3D 200) at a constant scan speed of 100 µm/s. Under these conditions, by decreasing the incoming laser average power, we are able to ablate stripes as narrow as 125 nm (with irregularities due to pulse-to-pulse instabilities) on thin metallic film-coated substrates [21] and 400 nm on graphene [19]. By changing the distance orthogonal to the ablation direction, micro- and nano-slit arrays are fabricated with different periods. Figure 2 shows an SEM image of a micro-slit array fabricated on graphene with this method for the periodicity of 10 µm using an average laser power of 0.25 mW. Note that due to multiple-ring structure of Bessel beams, it is not practical to have precise measurements of fluence. Hence, we report our measurements with measured average power. Using calculated Bessel beam profiles, we estimate that in our experimental setup, 0.1 mW average power (100 nJ pulse energy) corresponds to fluence of 130 mJ/cm^2 at the central lobe.

3 Analysis of SEM images

Scanning electron microscope provides detailed morphological and topographical information, allowing for both high magnification and excellent depth of field. Since SEM images are intensity maps of electrons being deflected toward the secondary electron detector and electrons do not have colors, they are normally grayscale images.

If any SEM image of an ablated sample is carefully examined, it is observed that some regions are accidentally ablated, whereas the laser is unable to ablate some other targeted spots. All over- and under-ablated regions must be identified in order to quantify ablation quality. In this work, we achieve such quantification by analyzing these grayscale SEM images with MATLAB. Note that the binary

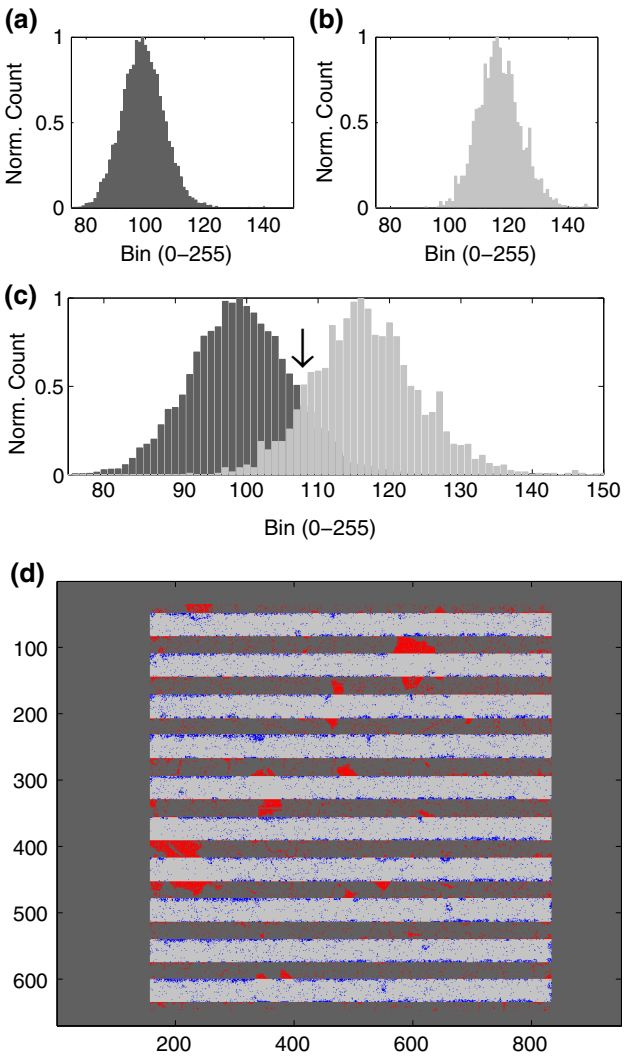

Fig. 3 Histogram analyses of **a** untouched and **b** ablated regions marked by *red* and *green dashed lines* in Fig. 2; **c** overlapped histograms to find out the threshold value, δ_t, marked by the *arrow*; **d** successfully ablated (*light gray*), under-ablated (*blue*), and over-ablated (*red*) regions around the ablated channels determined using δ_t

representation assumes that 0 is black and 255 is white for our 8 bit per pixel images.

In the first step, histogram analysis is performed on reference ablated and untouched regions, as shown in Fig. 3a, b. These reference regions are marked with dashed red and green lines in Fig. 2. The average pixel values of these untouched and ablated regions are 98 and 116, respectively. In Fig. 3c, we overlap these analyses and choose the intersection value of 107 (marked by the arrow) as a threshold value (δ_t) to delineate the untouched and ablated pixels. Similar histogram analysis is done for the white spots (debris), and we conclude that these unwanted regions have the pixel values of 240 or higher. We take this value as a debris threshold, (δ_d), and we exclude all the pixels exceeding δ_d from our analyses since they are neither untouched nor ablated spots. Hence, if A matrix represents this grayscale SEM image, it is assumed that any element of A, which is larger than δ_t and smaller than δ_d, represents an ablated region. Similarly, any element of A, which is smaller than or equal to δ_t is assume to represent an untouched region. Under-ablated and over-ablated spots (pixels) are marked with blue and red, respectively, in Fig. 3d, where light grays represent successfully ablated spots.

In the second step, we calculate the sum of the pixel values line by line. As shown in Fig. 4a, this simple calculation provides an average vertical profile, which is very useful to identify ablated channels. The center and width of the each ablated channel are calculated using this profile and the scale bar provided in the original SEM image. Note that since the lighter regions of the SEM image are the ablated ones, they have higher values in the 8 bit representation and hence in Fig. 4a, which looks like a rectangular pulse train, those pulses correspond to ablated spots. An interesting observation is that there is a dip at the center of the each pulse if the average power (P_{av}) is ~ 0.25 mW or higher. Micro-Raman measurements taken at the center of ablated channels exhibit a small drop in the Si peak at 520 cm^{-1} (see [19] for further discussions and Raman spectra). From this, we conclude that for $P_{av} \geq 0.25$ mW, the energy of the pulse is sufficiently high that even after nonlinear absorption by graphene layer, the transmitted pulse energy is still above the ablation threshold of Si and starts to damage the substrate.

In the third and final step, we aim to quantify the quality of the ablation process, which could be considered as AFOM. If we simply calculate the ratio of accurately ablated spots (pixels) to the whole image, AFOM of a totally ablated sample would be very high even though it is far from the desired pattern. If we calculate the ratio of sum of accurately ablated and untouched pixels to the whole image, then the AFOM of an untouched sample would be extremely high, which should not be the case. Or if we simply do the same calculation over a narrower region of the SEM image covering the ablation area without taking number of ablated channels into account, we might end up with another totally wrong AFOM. This is why we calculate the AFOM by averaging the success of each ablation channel as follows. We first choose a region surrounding each ablation channel, as shown with red dashed lines in Fig. 4b. The width of this region is the minimum of half period (which is 5 μm in this case) and ablation channel width. This choice provides an objective measure considering the decreasing ratio of ablated region to untouched region when the beam intensity is near threshold level. Then, for each channel, we calculate both the ratio of accurately ablated pixels to those targeted for ablation and the ratio of untouched to untargeted pixels. The AFOM, in other words the overall success of the ablation process, is calculated by taking average of the multiplication of these numbers, i.e.,

$$\mathrm{AFOM} = \frac{100}{N_{\mathrm{ch}}} \times \sum_{i=1}^{N_{\mathrm{ch}}} \left(\frac{p_{\mathrm{aa,i}}}{p_{\mathrm{ar,i}}}\right) \times \left(\frac{p_{\mathrm{au,i}}}{p_{\mathrm{ur,i}}}\right) \quad (1)$$

where

N_{ch}: number of ablated channels,
$p_{\mathrm{aa,i}}$: number of accurately ablated pixels on the ablation channel-i,
$p_{\mathrm{ar,i}}$: number of pixels on the ablation channel-i,
$p_{\mathrm{au,i}}$: number of untouched pixels surrounding channel-i,
$p_{\mathrm{ur,i}}$: number of pixels surrounding channel-i.

By multiplying these two ratios, this formula provides a number that effectively measures the accuracy with which each channel is ablated, but is not skewed by having a high ratio of targeted to untargeted surface area, as would occur with weighted averaging. For example, if a channel is created with 10 % mis-ablation and 10 % over-ablation, the AFOM is 81 % $(100 \times (1 - 0.1) \times (1 - 0.1) = 81)$, which is a meaningful number to rate the overall ablation quality. It should be also noted that the pixel resolution in our SEM images changes between 80 nm/pixel to 120 nm/pixel depending on the imaging parameters. The utilized cubical interpolation method assures an error less than 20 nm/pixel. SEM images with higher resolution increase the accuracy of AFOM calculations.

Theoretically, ablation width (d) can be estimated by calculating the diameter value $(d = 2r)$ satisfying $P(r) > P_t$, where P_t is the minimum power required for ablation for chosen beam profile and $P(r)$ is the average power of the laser pulse at a distance r with respect to beam axis [18, 24]. Blue solid line in Fig. 5a shows our theoretical estimates obtained assuming a threshold fluence

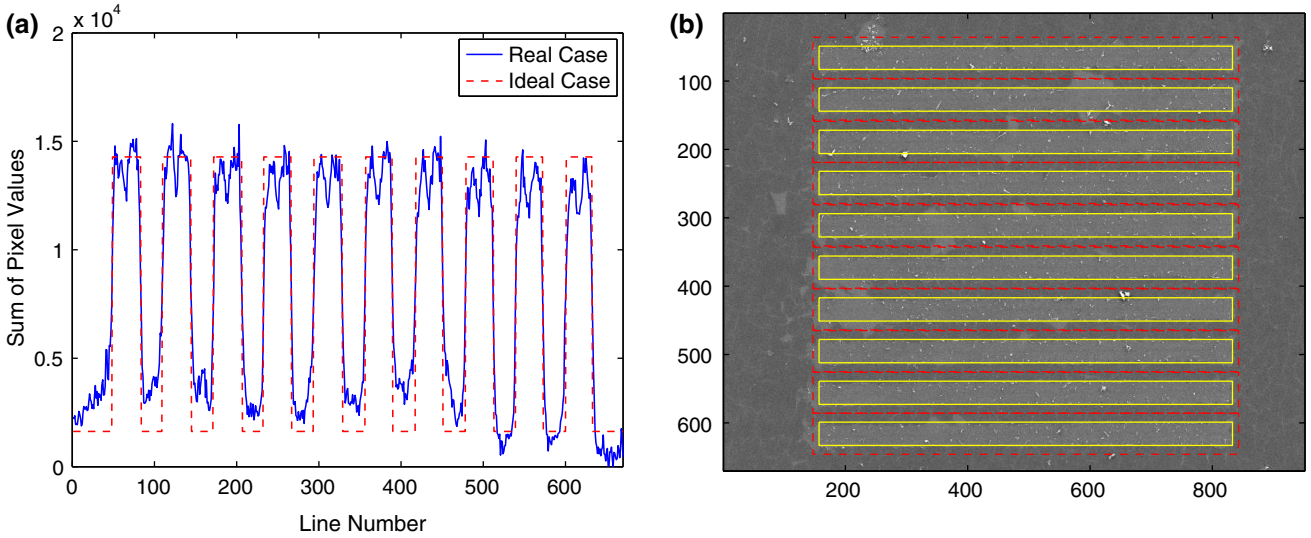

Fig. 4 **a** Average vertical profile. **b** Cropped version of Fig. 2, where the regions surrounded with *yellow lines* are ablated stripes

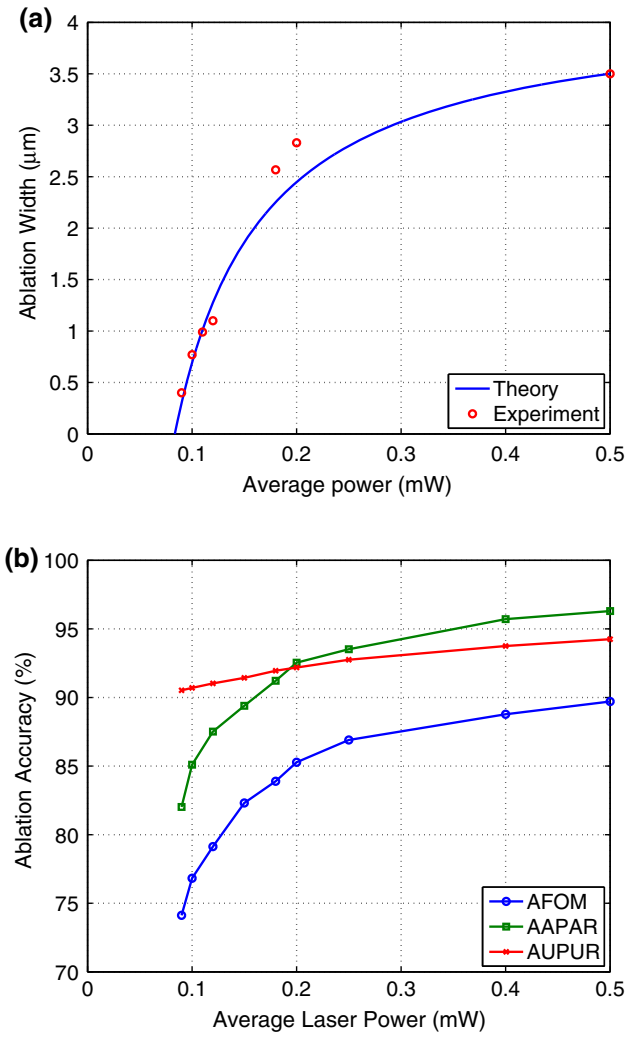

Fig. 5 Average laser power versus **a** ablation width and **b** ablation quality, where AAPAR is accurately ablated pixels in ablation regions and AUPUR is accurately untouched pixels in untouched regions

value of 115 mJ/cm^2 for graphene. In the same figure, we also mark our experimental results (showing a reduction in average ablation width from 3.5 μm to 400 nm) with red circles and overall there is a very good agreement. Further ablation width reduction is possible in a clean room-like environment by decreasing the room temperature, laser instability and unwanted vibrations and by utilizing more precise stages and amplifiers.

In Fig. 5b, we plot the AFOM as a function of beam intensity calculated using the explained procedure and the developed AFOM formula. In the same figure, we also plot the percentiles of accurately ablated pixels in ablation regions (AAPAR) and accurately untouched pixels in untouched regions (AUPUR). Clearly, as beam intensity is decreased, ablation accuracy decreases as well. This trade-off is expected and natural outcome of ablation near threshold. When one works very close to ablation threshold, minute changes in pulse fluence can significantly alter ablation size. Since over-ablation is mainly controlled by setup (system vibrational) stability, it is less affected by the beam intensity change compared to under-ablation, which heavily depends on shot-to-shot stability of the laser. In other words, aforementioned environmental conditions to decrease the ablation width are also expected to decrease AUPUR and similarly increased precision over laser power and scanning are expected to decrease AAPAR.

4 Conclusion

A simple yet accurate model is developed to quantify the ablation quality of graphene-coated substrates. Numerical analyses reveal that fs-laser ablation can be used to create nano-size features on single-layer graphene with $\sim$75 %

accuracy in ambient conditions. This same methodology can be applied to other graphene-like atomically thin-layered materials.

Acknowledgments This work was supported by Scientic and Technological Research Council of Turkey (TUBITAK, Grant No. 110T330) and Turkish Academy of Sciences (TUBA GEBIP). R. Sahin also thanks TUBITAK for PhD scholarship.

References

1. A.K. Geim, Graphene: status and prospects. Science **324**(19), 1530–1534 (2009)
2. A.K. Singh, B.I. Yakobson, Electronics and magnetism of patterned graphene nanoroads. Nano Lett. **9**(4), 1540–1543 (2009)
3. P. Avouris, Graphene: electronic and photonic properties and devices. Nano Lett. **10**(11), 4285–4294 (2010)
4. F. Bonaccorso, Z. Sun, T. Hasan, A.C. Ferrari, Graphene photonics and optoelectronics. Nat. Photonics **4**, 611–622 (2010)
5. K.S. Novoselov, V.I. Falko, L. Colombo, P.R. Gellert, M.G. Schwab, K. Kim, A roadmap for graphene. Nature **490**(7419), 192–200 (2012)
6. Z. Chen, Y.-M. Lin, M.J. Rooks, P. Avouris, Graphene nanoribbon electronics. Phys. E **40**, 228–232 (2007)
7. M.Y. Han, B. Ozyilmaz, Y.B. Zhang, P. Kim, Energy band-gap engineering of graphene nanoribbons. Phys. Rev. Lett. **98**, 206805 (2007)
8. R. Yang, Z.W. Shi, L.C. Zhang, D.X. Shi, G.Y. Zhang, Observation of Raman G-Peak split for graphene nanoribbons with hydrogen-terminated zigzag edges. Nano Lett. **11**(10), 4083–4088 (2011)
9. H.O. Jeschke, M.E. Garcia, K.H. Bennemann, Theory for the ultrafast ablation of graphite films. Phys. Rev. Lett. **87**(1), 015003 (2001)
10. Y. Zhang, L. Guo, S. Wei, Y. He, H. Xia, Q. Chen, H.-B. Sun, F.-S. Xiao, Direct imprinting of microcircuits on graphene oxides film by femtosecond laser reduction. Nano Today **5**(1), 15–20 (2010)
11. G. Kalita, L. Qi, Y. Namba, K. Wakita, M. Umeno, Femtosecond laser induced micropatterning of graphene film. Mater. Lett. **65**, 1569–1572 (2011)
12. S. Dhar, A. Roy Barman et al., A new route to graphene layers by selective laser ablation. AIP Adv. **1**, 022109 (2011)
13. W. Zhang, L. Li, Z.B. Wang, A.A. Pena, D.J. Whitehead, M.L. Zhong, Z. Lin, H.W. Zhu, Ti: sapphire femtosecond laser direct micro-cutting and profiling of graphene. Appl. Phys. A **109**(2), 291–297 (2012)
14. A. Roberts, D. Cormode, C. Reynolds, T. Newhouse-Illige, B.J. LeRoy, A.S. Sandhu, Response of graphene to femtosecond high-intensity laser irradiation. Appl. Phys. Lett. **99**, 051912 (2011)
15. R.J. Stohr, R. Kolesov, K. Xia, J. Wrachtrup, All-optical high-resolution nanopatterning and 3D suspending of graphene. ACS Nano **5**(6), 5141–5150 (2011)
16. J.-H. Yoo, J.B. In, J.B. Park, H. Jeon, C.P. Grigoropoulos, Graphene folds by femtosecond laser ablation. Appl. Phys. Lett. **100**, 233124 (2012)
17. M. Currie, J.D. Caldwell, F.J. Bezares, J. Robinson, T. Anderson, H. Chun, M. Tadjer, Quantifying pulsed laser induced damage to graphene. Appl. Phys. Lett. **99**, 211909 (2011)
18. F. Courvoisier, J. Zhang, M.K. Bhuyan, M. Jacquot, J.M. Dudley, Applications of femtosecond Bessel beams to laser ablation. Appl. Phys. A Mater. Sci. Process. **112**(1), 29–34 (2013)
19. R. Sahin, E. Simsek, S. Akturk, Nanoscale patterning of graphene through femtosecond laser ablation. Appl. Phys. Lett. **104**, 053118 (2014)
20. B. Yalizay, T. Ersoy, B. Soylu, S. Akturk, Fabrication of nanometer-size structures in metal thin films using femtosecond laser Bessel beams. Appl. Phys. Lett. **100**, 031104 (2012)
21. R. Sahin, Y. Morova, E. Simsek, S. Akturk, Bessel-beam-written nanoslit arrays and characterization of their optical response. Appl. Phys. Lett. **102**(19), 193106 (2013)
22. A.C. Ferrari, J.C. Meyer, V. Scardaci, C. Casiraghi, M. Lazzeri, F. Mauri, S. Piscanec, D. Jiang, K.S. Novoselov, S. Roth, A.K. Geim, Raman spectrum of graphene and graphene layers. Phys. Rev. Lett. **97**, 187401 (2006)
23. X. Li, Y. Zhu, W. Cai, M. Borysiak, B. Han, D. Chen, R.D. Piner, L. Colombo, R.S. Ruoff, Transfer of large-area graphene films for high-performance transparent conductive electrodes. Nano Lett. **9**(12), 4359–4363 (2009)
24. J. Arlt, K. Dholakia, Generation of high-order Bessel beams by use of an axicon. Opt. Commun. **177**(1–6), 297–301 (2000)